A Geant4 tool for edge-illumination X-ray phase-contrast imaging

L. Brombal,[a,*] **L. Rigon,**[a,b] **F. Arfelli,**[a,b] **R.H. Menk**[a,c] **and F. Brun**[a,d]

[a] *Division of Trieste, National Institute for Nuclear Physics (INFN), Via. A. Valerio 2, 34127 Trieste, Italy*
[b] *Department of Physics, University of Trieste, Via A. Valerio 2, 34127 Trieste, Italy*
[c] *Elettra Sincrotrone S.C.p.A., s.s. 14 km 163500 in Area Science Park, 34149 Basovizza Trieste, Italy*
[d] *Department of Engineering and Architecture, University of Trieste, Via A. Valerio 6, 34127 Trieste, Italy*

E-mail: luca.brombal@ts.infn.it

ACCEPTED: *December 6, 2021*

ABSTRACT: The PEPI project is developing a new experimental facility integrating a chromatic photon-counting detector within an edge-illumination (EI) phase-contrast setup. In this context, a novel Geant4-based simulation tool has been introduced with the aim of defining the optimal design of the experimental setup. The code includes a custom X-ray refraction process and allows simulating the whole EI system, comprising a polychromatic and extended source, absorbing masks, substrates, their movement during acquisition, and X-ray detection. In this paper, a realistic spectral detector model is introduced and its energy response validated against experimental data acquired with synchrotron radiation at energies between 26 and 50 keV. Moreover, refraction and transmission images of a plastic phantom are reconstructed from simulation data and successfully compared with theoretical predictions. Finally, an optimization study aiming at finding the effect of the X-ray focal spot size (i.e. spatial coherence) on image quality is presented; the results suggest that, in the considered configuration, the system can tolerate source sizes up to 30 µm, while, for a fixed exposure time, the best signal-to-noise ratio in refraction images is found for source sizes in the order of 10 to 15 µm.

KEYWORDS: Multi-modality systems; Simulation methods and programs; X-ray detectors; X-ray radiography and digital radiography (DR)

*Corresponding author.

Contents

1 Introduction

The signal formation in conventional X-ray imaging relies on the attenuation of the incoming radiation traversing the investigated sample. While providing adequate information in many applications, from diagnostic imaging to industrial inspection, the contrast generated by attenuation is often insufficient to distinguish objects composed of low-Z materials such as soft tissues or plastics. Additionally, moving to the high-end of the energy spectrum used in most radiological applications (10–100 keV), the contrast is further reduced by the steep dependence of attenuation coefficients on the energy. For these reasons, many efforts are devoted towards the development of techniques sensitive to the phase-shift accumulated by X-rays through the object [1].

Phase effects are related to the real decrement (δ) of the refractive index (n) characterizing the investigated sample, whereas attenuation is linked to its imaginary part (β). In the case of light materials, δ is two to three orders of magnitude higher than β, therefore phase effects dominate over attenuation. Since X-ray detectors are not directly sensitive to phase, the role of X-ray phase-contrast imaging (XPCI) is to convert phase-shift effects into detectable intensity modulation. Pioneered two decades ago within synchrotron radiation facilities, XPCI is now becoming widely used also with conventional X-ray sources [2, 3]. The transition from the synchrotron to a compact laboratory environment requires relaxation in terms of requirements on the source coherence, both spatial and temporal. In this context, two XPCI techniques, namely edge illumination (EI) [4] and Talbot-Lau grating interferometry (GI) [5], have succeeded in this transition, and an increasing number of applications, ranging from biomedical imaging to material science, is being documented in the scientific literature.

Independently from XPCI, recent years have witnessed unprecedented development in the field of hybrid X-ray imaging detectors. Novel devices have both led to major advantages over

conventional indirect conversion detectors, such as higher efficiency and/or higher spatial resolution, and opened up entirely new possibilities, such as pixel-based energy discrimination of photons, spectral performances, and super-resolution imaging [6].

In this framework, the INFN-funded PEPI (Photon-counting Edge-illumination Phase-contrast Imaging) project is developing a new experimental facility integrating a photon-counting hybrid detector (Pixirad-PixieIII [7]) within an EI phase-contrast setup. The aim of the project is to combine the specific advantages of the detector, namely high efficiency, sharp response, and spectral capabilities, with the sensitivity to phase effects (i.e., refraction and ultra-small-angle scattering) enabled by EI. In order to define the optimal design of the experimental setup, a novel publicly available Geant4-based simulation platform (Geant4PEPI) has been developed [8]. Within this tool phase effects are simulated through a custom X-ray refraction process, that is not included in the available Geant4 releases, and an EI experimental setup is replicated including realistic source spatial and spectral distributions, geometry and compositions of samples and absorbing masks, and image acquisition procedures [9].

In this paper, the first results on the PEPI's setup optimization based on the simulation are presented. In particular, the study will focus on the dependence of the quality of phase-contrast images (refraction and transmission), measured in terms of signal-to-noise-ratio (SNR), on the X-ray focal spot size. Additionally, a model of a photon-counting detector with a realistic energy response included in the simulation is introduced as well as its validation against synchrotron-based experimental data acquired with the Pixirad CdTe hybrid pixel detector.

2 Materials and methods

2.1 Edge illumination

Edge illumination is a non-interferometric XPCI technique that, in its most common implementation, makes use of two periodic absorbing grids or masks positioned upstream from the sample (sample mask) and the detector (detector mask), respectively, as depicted in panel (a) of figure 1 [4]. The sample mask structures the X-ray beam into a series of independent beamlets. Upon the interaction with the sample, each beamlet is attenuated, deviated and diffused due to the X-ray attenuation, refraction, and ultra-small-angle scattering (USAXS) properties of the sample. Before interacting with the detector, the beamlets are partially intercepted by the detector mask that, apart from the magnification scaling factor, is identical to the sample mask and matches the detector's pixel pitch. By laterally displacing the two masks and acquiring two (or more) images at different displacement positions it is possible to uncouple attenuation/transmission, refraction, and (optionally) USAXS signals, therefore obtaining parametric images of complementary sample's properties. In order for the reconstruction to be quantitative, the system must be previously characterized, i.e. its illumination curve (IC) must be known. The IC is obtained by finely scanning one mask with respect to the other and recording the detected intensity for each lateral position (panel (b) in figure 1). Mathematically, the illumination curve is given by the convolution of the two masks aperture functions, usually represented as box functions, and the X-ray source intensity spatial distribution [10]. Once the IC is known, the parametric images of refraction (α) and transmission (T) can be obtained from two images acquired at displacements corresponding

to the opposite slopes of the IC, similarly to the diffraction enhanced imaging case [11], as:

$$\alpha = \frac{m}{z_{\mathrm{od}}} \frac{I_2 C_1 - I_1 C_2}{I_1 \dot{C}_2 - I_2 \dot{C}_1} \tag{2.1}$$

$$T = \frac{I_1 \dot{C}_2 + I_2 \dot{C}_1}{C_1 \dot{C}_2 - C_2 \dot{C}_1} \tag{2.2}$$

where $I_{1,2}$ are the images at displacement positions 1 and 2 (referred to as working points), $C_{1,2}$ are the values of the illumination curve, $\dot{C}_{1,2}$ its first derivative, z_{od} the object to detector distance and m the magnification factor, and the operations on images are intended as pixel-by-pixel. It is worth noting that the IC fully determines the performances of the system in terms of sensitivity and dynamic range [12]. Specifically, sharper ICs correspond to higher angular sensitivity and lower maximum detectable refraction angles.

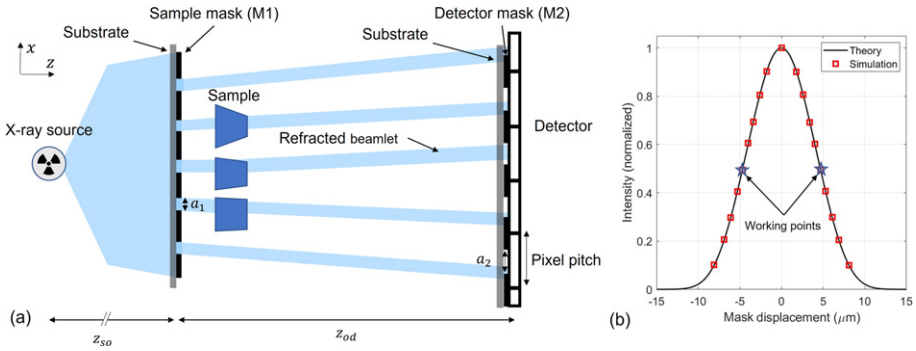

Figure 1. Top view sketch of the simulated EI setup (a); a comparison between the theoretical (solid line) and simulated (squares) IC (b).

2.2 Geant4PEPI simulation

When the spatial coherence of the experimental setup is limited, such as in the case of compact laboratory-based systems, simple geometrical ray-tracing models can accurately describe the formation of phase-contrast signals without the need for rigorous wave propagation models [13]. For this reason, Monte Carlo (MC) platforms such as Geant4, which intrinsically treat all particles (including photons) with a ray-tracing approach, can be used to simulate non-interferometric phase-contrast systems. Specifically, in the Geant4PEPI framework, phase effects are simulated through the implementation of the X-ray refraction process (`PepiXrayRefraction` class), which is an extension to X-ray energies of the Snell's law. Similar approaches have already been documented in other MC X-ray transport codes (FLUKA [14]), or Geant4-based wrappers (GATE [15], and GAMOS [16]), but no dedicated classes presently exist in the Geant4 kernel. Since refractive indices of elements, materials, and compounds are not directly available in Geant4 at X-ray energies, they have been supplied externally from the TS imaging database [17] and they have been associated to the various materials by adding a new property (`RINDEX`) through the `G4MaterialPropertiesTable` class.

Geant4PEPI includes the implementation of a complete EI system, containing a polychromatic tungsten anode spectrum and extended X-ray source, sample and detector masks made of gold and respective silicon substrates, a test object made of 3 trapezoidal prisms with different inclinations and a pixellated CdTe sensor with a thickness of 650 µm, mimicking the Pixirad detector (see panel (a) of figure 1). Through dedicated `Messenger` classes the user can change the X-ray tube voltage, in the interval 40–100 kV at 10 kV steps, the system magnification, the masks apertures, pitches and thickness, and the detector threshold. Moreover, the user can select any desired displacement between M1 and M2, therefore any working point in the IC, and acquire simulated IC curves by displacing the sample out from the field of view (see panel (b) of figure 1).

2.3 Detector energy response

With the aim of matching the energy response of a photon-counting detector, a dedicated primitive scorer class (`PepiPsPixirad`) has been included in the Geant4PEPI framework. In this class, each detector unit (pixel) records all the energy released for each event. When a single event, i.e. impinging photon, releases its energy in more than one pixel, typically due to the production of fluorescence photons and high-energy photoelectrons, a clustering mechanism among neighboring pixels is triggered. The clustering mechanism looks for the energy releases in the three closest pixels, sums them all, and assign the whole energy to the pixel where the highest fraction of energy was released. This mechanism is analogous to charge summing modes encountered in advanced chips such as Medipix3 [18] and PixieIII [7]. The energy deposit is then compared to a threshold value and, if it exceeds the threshold, a count is assigned to the pixel. In order to take into account the actual energy resolution of the detector, that is influenced by both the statistics associated with the electron-hole pairs formation in the sensor and inhomogeneities in the thresholds among pixels, the energy threshold value is chosen to be a random number that fluctuates with a Gaussian distribution around a user-defined mean value. The full-width-half-maximum (FWHM) of this fluctuation is an energy-dependent value, comprised between 3 and 4 keV, given by the characterization measurements performed by Di Trapani et al. [19].

To validate the scoring approach implemented in the simulation, a comparison against experimental data acquired with monochromatic synchrotron radiation has been performed. From the differential spectrum plots reported in figure 2, it is clear that the simulation adequately reproduces all the spectral features observed experimentally. In particular, for X-ray energies above k-electrons binding energies of CdTe (26.7 keV for cadmium and 31.8 keV for tellurium), fluorescence and escape peaks start appearing in the spectra and they are well-matched by simulations both in terms of energy and peak height.

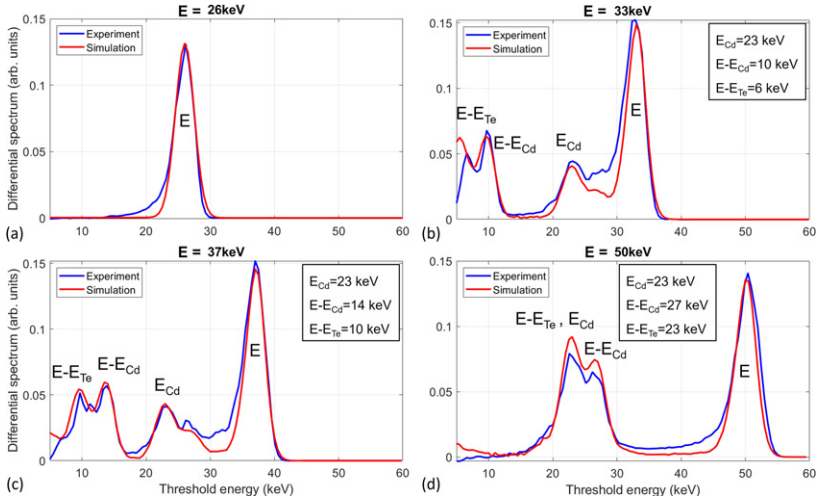

Figure 2. Comparison between experimental (blue line) and simulated (red line) differential energy spectra at monochromatic energies of 26 keV (a), 33 keV (b), 37 keV (c) and 50 keV (d). Experimental data are taken from Di Trapani et al. [19].

2.4 Simulation parameters and data analysis

The simulations presented in this paper were carried out to understand the impact of the X-ray focal spot size on the quality of refraction and transmission images. The simulation parameters are reported in table 1. For each focal spot size, two sample images were produced at opposite sides of the IC corresponding to the 50% intensity with a statistics of 2×10^9 photons, while the detector threshold was set to 10 keV. It is worth mentioning that, since the IC width depends on the focal spot size, for each simulation different displacements of the masks were used ranging from ±4 µm for the smallest focal spot of 2.5 µm (FWHM, Gaussian distribution), to ±13 µm for the largest focal spot of 50 µm. Refraction and transmission images were then obtained from the simulated images according to equations (2.1) and (2.2). The signal-to-noise-ratio (SNR) for refraction images was computed as [20]:

$$\mathrm{SNR}_\alpha = \frac{|\bar{\alpha}_+| + |\bar{\alpha}_-|}{2\sigma_\mathrm{b}} \tag{2.3}$$

where $\bar{\alpha}_+$ and $\bar{\alpha}_-$ are the mean values of the positive and negative refraction signals of the central trapezoid, while σ_b is the standard deviation measured in the background. The SNR for transmission images was computed as:

$$\mathrm{SNR}_T = \frac{|\bar{T}_\mathrm{c} - \bar{T}_\mathrm{b}|}{\sigma_\mathrm{b}} \tag{2.4}$$

where $\bar{T}_\mathrm{c}$ and $\bar{T}_\mathrm{b}$ are the mean intensity computed at the center of the central trapezoid and in the background, respectively, while σ_b is the standard deviation measured in the background. For each image, SNR values are calculated on 5 sets of non-overlapping region-of-interest (ROIs) and the associated uncertainty is computed as the standard deviation of the measurements. The ROIs are displayed in figure 3.

Table 1. Simulation parameters.

Spectrum	**Focal size**	**Object-detector distance**	**Magnification**
W – 40 kV – 2 mm Al	2.5 – 50 µm	0.5 m	2
M1 pitch/aperture	**M2 pitch/aperture**	**Mask/substrate thickness**	**Mask/substrate material**
31/7.5 µm	62 /15 µm	250/525 µm	gold/silicon

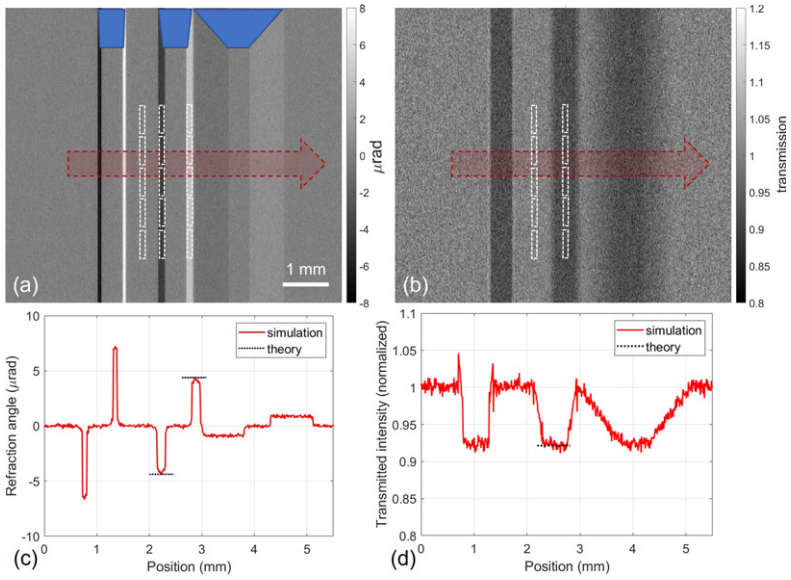

Figure 3. Refraction (a) and transmission (b) obtained from the simulation and their respective intensity profiles in (c) and (d) calculated along the direction expressed by the arrows in (a) and (b). Region of interests for SNR measurements are reported as dashed boxes in (a) and (b), while the inset in (a) depicts the top view of the simulated sample.

3 Results and discussion

3.1 Refraction and attenuation images: simulation vs. theory

Panels (a) and (b) of figure 3 show respectively the reconstructed refraction and transmission images obtained with a simulated focal spot size of 10 µm FWHM. As expected, in the refraction image symmetric positive and negative signals are visible in correspondence to the inclined sides of the trapezoids, whereas the transmission image shows increasing X-ray attenuation moving towards the center of each trapezoid. From both the images and the line profiles reported in panels (c) and (d), it can be noticed that the refraction image has a much smaller noise content and a higher SNR. Moreover, the comparison between simulated and theoretical signal intensity shows a good agreement both for refraction and transmission, also demonstrating the correctness of the refraction process implemented in the simulation.

3.2 The effect of the source size

In figure 4 refraction (top row) and transmission (bottom row) images obtained from simulations at different source sizes, from 2.5 to 50 µm FWHM, are reported. Focusing on refraction images, it is clear that larger focal spot sizes correspond to an increase in image noise. This behavior is expected as large focal spot sizes result in a shallow IC and, therefore, to a reduced refraction sensitivity. Additionally, when the focal spot size projected at sample position exceeds the spacing between consecutive mask apertures, as in the case of the largest focal spot (50 µm), the reconstruction of refraction signal loses its quantitativeness and severe artifacts are introduced. This is due to the fact that, as a consequence of the focal spot penumbra, consecutive beamlets cannot be considered independent, i.e. cross-talk sets in, and therefore the image reconstruction model of equation (2.1) is no longer valid. On the other hand, considering transmission images (bottom row), the effect of source size is less pronounced and, apart from mild artifacts appearing at the edges of the trapezoids at larger source sizes, image quality is approximately constant.

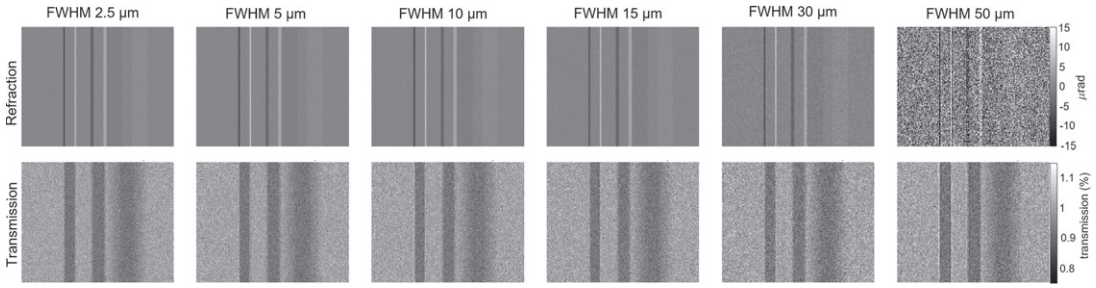

Figure 4. Reconstructed refraction (top row) and transmission (bottom row) images simulated at different source sizes, from 2.5 (first column) to 50 µm FWHM (last column).

The qualitative analysis is confirmed by the SNR measurements performed on the central trapezoid and shown in panel (a) of figure 5. Interestingly, for the smallest source size, the refraction SNR is a factor of 5 higher than the transmission SNR. As the source size gets larger, refraction SNR is reduced down of a factor of 20 at the largest focal spot, going below the transmission SNR for focal sizes between 30 and 50 µm. Conversely, transmission SNR values are loosely dependent on the source size and maximum variations in the order of 40% are observed.

From these findings it might seem that it is best to keep the focal spot as small as possible in an EI setup, such as in the case of simulated data, where a fixed number of photons was considered in each simulation. This consideration holds as long as constraints in terms of dose are present, i.e. when the X-ray fluence delivered to the sample must be as low as possible. On the other hand, when privileging a short exposure time, larger focal spot sizes can be desirable. In fact, X-ray sources with larger focal spot delivers higher flux meaning that, for a fixed exposure time, statistical noise is decreased. Specifically, for many commercially available X-ray tubes, the focal spot size is directly proportional to the power delivered to the anode hence, at a constant tube voltage, to the X-ray flux. Considering that for systems dominated by statistical noise, such as in the case of photon-counting detectors, the SNR is directly proportional to the square root of the flux, one can write:

$$\mathrm{SNR} \propto \sqrt{\mathrm{flux}} \propto \sqrt{\mathrm{source\ size}}. \tag{3.1}$$

This dependence has been factored in the calculation of the SNR, as reported in panel (b) of figure 5. From the plot is interesting to observe that refraction SNR is no longer a monotonically decreasing function and, for a fixed exposure time, image quality is maximized for source sizes between 10 and 15 µm. At the same time, transmission SNR becomes a monotonically increasing function whose trend is dominated by the photon statistics ($\propto \sqrt{\text{flux}}$).

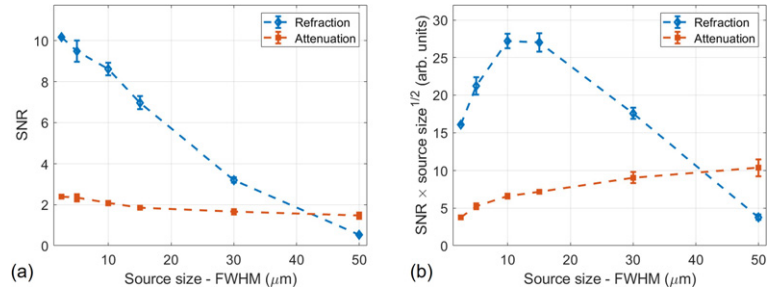

Figure 5. In (a) the progression of refraction and transmission SNR as a function of the X-ray source size. In (b) SNR values are multiplied to the square root of the source size to account for the dependence between SNR, X-ray flux, and source size.

4 Conclusions

This paper reported the first results obtained with a novel Geant4-based simulation platform dedicated to edge-illumination phase-contrast imaging. The developed code allows the simulation of a complete EI setup, ranging from the source size and spectrum to the mask parameters and detector response. Specifically, a detector response model for simulating the spectral performances of a chromatic photon-counting detector (Pixirad-PixieIII) has been implemented and validated against experimental data. Refraction and transmission images of a virtual plastic phantom were obtained and good correspondence with theoretical value was found. An optimization study in terms of image quality as a function of the X-ray focal spot size was performed demonstrating that, for a fixed exposure time, spot sizes around 10 to 15 µm maximize the refraction signal-to-noise ratio in the studied configuration. The developed simulation code, that will be extensively used in the development of a novel edge-illumination facility, is intended as a flexible platform for phase-contrast setups optimization and is made publicly available.

Acknowledgments

This work is carried out in the framework of the PEPI project, supported by Istituto Nazionale di Fisica Nucleare (National Scientific Commission 5 for Technological and Inter-disciplinary Research, No. 22260/2020).

References

[1] A. Bravin, P. Coan and P. Suortti, *X-ray phase-contrast imaging: from pre-clinical applications towards clinics, Phys. Med. Biol.* **58** (2012) R1.

[2] M. Endrizzi, *X-ray phase-contrast imaging*, *Nucl. Instrum. Meth. A* **878** (2018) 88.

[3] L. Brombal et al., *Monochromatic propagation-based phase-contrast microscale computed-tomography system with a rotating-anode source*, *Phys. Rev. Appl.* **11** (2019) 034004.

[4] A. Olivo and R. Speller, *Modelling of a novel X-ray phase contrast imaging technique based on coded apertures*, *Phys. Med. Biol.* **52** (2007) 6555.

[5] F. Pfiffer et al., *Phase retrieval and differential phase-contrast imaging with low-brilliance X-ray sources*, *Nat. Phys.* **2** (2006) 258.

[6] R. Ballabriga et al., *Review of hybrid pixel detector readout ASICs for spectroscopic X-ray imaging*, 2016 *JINST* **11** P01007.

[7] R. Bellazzini et al., *PIXIE III: a very large area photon-counting CMOS pixel ASIC for sharp X-ray spectral imaging*, 2015 *JINST* **10** C01032.

[8] L. Brombal and F. Brun, *PEPI: Photon-counting Edge-illumination Phase-contrast Imaging*, https://web.infn.it/PEPI/ (2021).

[9] L. Brombal et al., *X-ray differential phase-contrast imaging simulations with Geant4*, *J. Phys. D.* **55** (2021) 045102.

[10] M. Endrizzi et al., *Hard X-ray dark-field imaging with incoherent sample illumination*, *Appl. Phys. Lett.* **104** (2014) 024106.

[11] D. Chapman et al., *Diffraction enhanced X-ray imaging*, *Phys. Med. Biol.* **42** (1997) 2015.

[12] P. Diemoz et al., *Sensitivity of laboratory based implementations of edge illumination X-ray phase-contrast imaging*, *Appl. Phys. Lett.* **103** (2013) 244104.

[13] A. Olivo and E. Castelli, *X-ray phase contrast imaging: from synchrotrons to conventional sources*, *Riv. Nuovo Cim.* **37** (2014) 467.

[14] S. Cipiccia et al., *Inclusion of coherence in Monte Carlo models for simulation of X-ray phase contrast imaging*, *Opt. Express* **22** (2014) 23480.

[15] M. Langer et al., *Towards Monte Carlo simulation of X-ray phase contrast using GATE*, *Opt. Express* **28** (2020) 14522.

[16] Z. Wang et al., *Implement X-ray refraction effect in Geant4 for phase contrast imaging*, *2009 IEEE Nuclear Science Symposium Conference Record (NSS/MIC)*, (2009), pp 2395–2398.

[17] T. Gureyev, *TS imaging*, http://ts-imaging.science.unimelb.edu.au/Services/Simple/ (2021).

[18] R. Ballabriga et al., *Medipix3: a 64 k pixel detector readout chip working in single photon counting mode with improved spectrometric performance*, *Nucl. Instrum. Meth. A* **633** (2011) S15.

[19] V. Di Trapani et al., *Characterization of the acquisition modes implemented in Pixirad-1/Pixie-III X-ray detector: effects of charge sharing correction on spectral resolution and image quality*, *Nucl. Instrum. Meth. A* **955** (2020) 163220.

[20] G. Kallon et al., *Comparing signal intensity and refraction sensitivity of double and single mask edge illumination lab-based X-ray phase contrast imaging set-ups*, *J. Phys. D* **50** (2017) 415401.